

Properties of ISM in two star-forming regions

Nikoghosyan E.*, Azatyan N., Harutyunian H., Baghdasaryan D., and Andreyan D.

Byurakan Astrophysical Observatory, 0213, Aragatsotn prov., Armenia

Abstract

The Hi-GAL provides an opportunity to make a complete and unbiased view of the continuum emission in the Galactic plane in five bands: 70, 160, 250, 350, and 500 μm . Our research focuses on two of star-forming regions. The first one is the molecular cloud, which includes G45.12+0.13 and G45.07+0.13 UC HII regions. Using the Modified blackbody fitting on *Herschel* images obtained in four bands: 160, 250, 350, and 500 μm , we determined the distribution of $N(\text{H}_2)$ hydrogen column density and T_d dust temperature. The maps of $N(\text{H}_2)$ and T_d show that UC HII regions clearly stand out against the general background of the molecular cloud with a relatively low density (from 1.0×10^{23} to $3.0 \times 10^{23} \text{ cm}^{-2}$) and significantly higher temperature (up to 100 K), what is fully consistent with the basic concept of UC HII regions about the presence of a hot, high mass stellar source and stellar wind, which leads to the blowing out of matter. The second one is the elongated star-forming region, which includes five stellar subgroups around IRAS 05184+3635, 05177+3636, 05168+3634, 05162+3639 and 05156+3643 sources. Here, on the contrary, the $N(\text{H}_2)$ is noticeably higher (from 1.0×10^{23} to $5.0 \times 10^{23} \text{ cm}^{-2}$) than in the surrounding molecular cloud and the T_d does not exceed 25 K.

Keywords: stars: pre-main sequence – infrared: stars – radiative transfer – ISM: hydrogen column density, dust temperature

1. Introduction

The Hi-GAL provides an opportunity to make a complete and unbiased view of the continuum emission in the Galactic plane in five bands: 70, 160, 250, 350, and 500 μm . This range of wavelengths covers the peak of the spectral energy distribution (SED) of the cold dust emission and makes it possible to determine such important parameters of Interstellar medium (ISM) as the $N(\text{H}_2)$ hydrogen column density and T_d dust temperature (Molinari et al., 2016).

For our study we choose two, relatively distant regions of star formation, which are different according to their properties and stellar content. The first is a pair of UC HII regions G45.07+0.13 and G45.12+0.13, associated with IRAS 19110+1045 and IRAS 19111+1048 sources, respectively (Wood & Churchwell, 1989). In Figure 1, we present the colour-composite image (left panel) with Hi-GAL three bands, where it is clearly seen that both regions are clearly distinguished by their brightness against the background of the surrounding molecular cloud. Moreover, it is clearly seen that they are connected by a relatively colder bridge. This can serve as further evidence that they belong to the same star-forming region and form a physically connected system. According to the results obtained in Han et al. (2015), the near and far kinematic distances of G45.07+0.13 and G45.12+0.13 regions are ~ 4.0 and ~ 8.0 kpc with tangent point distance of ~ 6 kpc. The last, far distance estimation, is better consistent with a more recent estimate according to the trigonometric parallax (7.75 ± 0.45 kpc) in Wu et al. (2019). Following them, we adopt a distance of 7.8 kpc in our study.

The next star-forming region is a molecular cloud surrounding the five IRAS sources: 05168+3634, 05184+3635, 05177+3636, 05162+3639, and IRAS 05156+3643 (Azatyan, 2019). The right panel of Figure 1 presents the colour-composite image with Hi-GAL three bands, where we can see that there are relatively hot gas-dust matter concentrations in the vicinity of all IRAS sources. The distance

*elena@bao.sci.am, Corresponding author

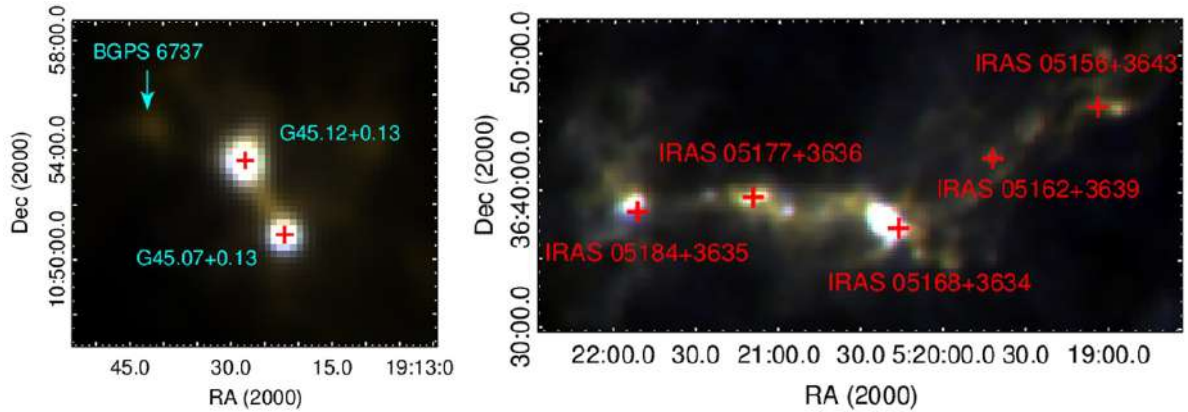


Figure 1. Colour-composite images with Hi-GAL three bands: PACS $160\ \mu\text{m}$ (blue), SPIRE $350\ \mu\text{m}$ (green), and $500\ \mu\text{m}$ (red). *Left panel:* G45.07+0.13 and G45.12+0.13 UCHII regions; *right panel:* IRAS 05168+3634 (Mol 9) star-forming region. The positions of IRAS sources are marked by crosses.

estimations of this region are controversial. A kinematic distance estimated by [Molinari et al. \(1996\)](#) is 6.08 kpc. The distance of IRAS 05168+3634 estimated according to a trigonometric parallax with VERA is 1.9 ± 0.2 kpc ([Sakai et al., 2012](#)). Such a large difference in the calculated distances determines a significant difference in the assessment of the mass of gas-dust matter. Therefore, for our calculations, we used both distance estimates.

The both star-forming regions are associated with different manifestations of activity, including maser and continual molecular emission, outflows, etc ([Varricatt et al., 2010](#), and ref. therein). Our previous studies shown that all IRAS sources in both star-forming regions are associated with dense young stellar clusters. The dense stellar clusters are associated with both G45.07+0.13 and G45.12+0.13 UCHII regions include a number of high-mass ZAMS stellar objects ([Azatyan et al., 2020](#), [Rivera-Ingraham et al., 2010](#), [Vig et al., 2006](#)). The molecular cloud in the second star-forming regions includes 240 candidates of YSOs within the radii of subclusters around all five IRAS sources. The age of the subclusters is estimated at 0.1-3 Myr ([Azatyan, 2019](#)).

2. Method

To obtain the physical parameters like $N(\text{H}_2)$ and T_d , the Modified single-temperature blackbody fitting, as well as the thermal emission from cold dust lying in the *Herschel* FIR optically thin bands ($160\text{--}500\ \mu\text{m}$) were used ([Hildebrand, 1983](#)). Following the discussion in the previous studies (e.g. [Battersby et al., 2011](#)), we excluded the $70\ \mu\text{m}$ observational data as the optically thin assumption would not hold. Besides, the emission here would have a significant contribution from the warm dust component, thus modelling with a single-temperature blackbody would over-estimate the derived temperatures. For initial *Herschel* images processing, which includes the elimination of bad pixels effect, the transformation of surface brightness units to Jy pixel^{-1} , as well as the convolution of images resolution to the $500\ \mu\text{m}$ image (the lowest among all images), we used the HIPE software.

The Modified single-temperature blackbody fitting, which was subsequently carried out on a pixel-by-pixel basis using the following formula:

$$S_\nu = B_\nu(\nu, T_d)\Omega(1 - e^{-\tau(\nu)}), \quad (1)$$

with

$$\tau(\nu) = \mu_{\text{H}_2} m_H k_\nu N(\text{H}_2), \quad (2)$$

where ν is the frequency, $S_\nu(\nu)$ is the observed flux density, $B_\nu(\nu, T_d)$ is the Planck function, Ω is the solid angle in steradians from where the flux is obtained (in this case for all bands the solid angle subtended by a $14\ \text{arcsec} \times 14\ \text{arcsec}$ pixel), $\tau(\nu)$ is the optical depth, μ_{H_2} is the mean molecular weight (adopted as 2.8 here), m_H is the mass of hydrogen, and k_ν is the dust opacity.

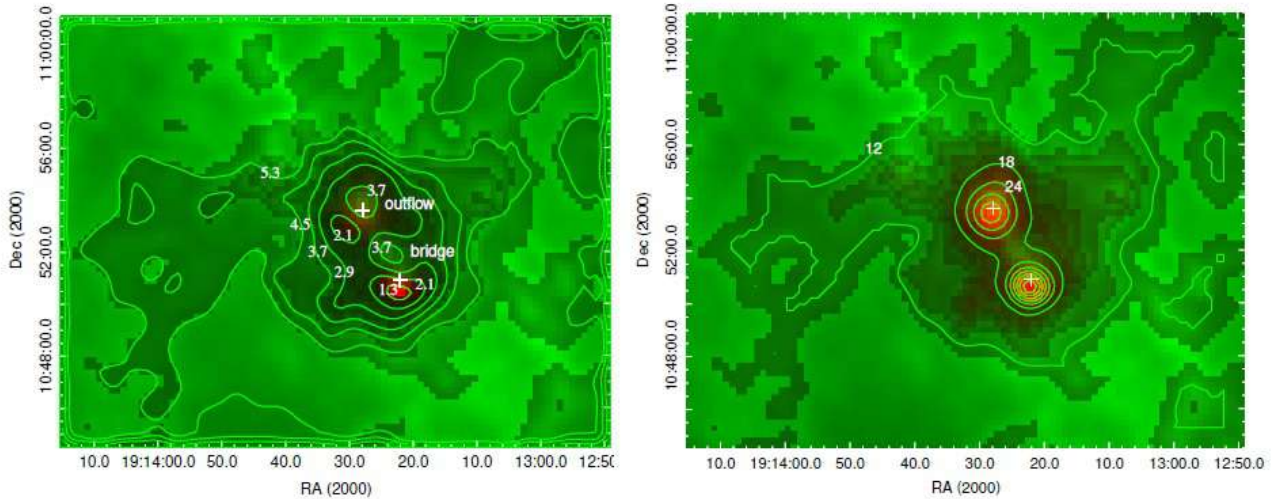


Figure 2. Colour-composite images of T_d (red) and $N(\text{H}_2)$ (green) distribution of the region surrounding G45.12+0.13 and G45.07+0.13 UC HII with overlaid contours of temperature in the left panel and $N(\text{H}_2)$ on the right panel. The temperature contours cover a range from 12 to 66 K with step in increments of 6 K. The $N(\text{H}_2)$ contours cover a range from 1.3×10^{23} to $5.3 \times 10^{23} \text{ cm}^{-2}$ with step in increments of $0.8 \times 10^{23} \text{ cm}^{-2}$. The positions of IRAS sources are marked by white crosses. On the right panel, the positions of G45.12+0.13 outflow and bridge between G45.12+0.13 and G45.07.0.13 UC HII are indicated (for more detail information see text).

For opacity, we adopted a functional form of $k_\nu = 0.1(\nu/1000 \text{ GHz})^\beta \text{ cm}^2 \text{ g}^{-1}$, with $\beta = 2$ (see Hildebrand, 1983). For each pixel, equation (1) was fitted using the four data points (160, 250, 350, and $500 \mu\text{m}$) keeping T_d and $N(\text{H}_2)$ as free parameters. Launhardt et al. (2013) used a conservative 15% uncertainty in the flux densities of the *Herschel* bands. We adopted the same value here for all bands. The uncertainties of the parameters were derived using Pearson's χ^2 statistics:

$$\chi^2 = \sum_{i=1}^N \frac{(D_i - F_i)^2}{F_i}, \quad (3)$$

where D_i is the observed flux and F_i is the flux predicted by the model, N is the number of bands.

From the derived column density values, we estimate the mass of the dusty clumps using the following expression:

$$M_{clump} = \mu_{\text{H}_2} m_H \text{Area}_{pix} \sum N(\text{H}_2), \quad (4)$$

where Area_{pix} is the area of a pixel in cm^2 .

3. Results

The results for both star-forming regions (see Sec. 1) are presented below.

3.1. G45.07+0.13 and G45.12+0.13 UC HII regions

The final obtained column density and dust temperature maps of the wider region surrounding G45.12+0.13 and G45.07+0.13 UC HII objects are shown in Figure 2. The map of temperature distribution clearly shows that the centers of both UC HII regions practically coincide with the temperature maxima, which reaches 49 K in G45.12+0.13 and 97 K in G45.07+0.13. On average, in the vicinity of IRAS 19110+1045, the value of $N(\text{H}_2)$ is $\sim 2 \times 10^{23} \text{ cm}^{-2}$, which is well coincides with the data in Churchwell et al. (2010) and almost an order of magnitude less than it was estimated from the 1.3 mm dust emission in Hernández-Hernández et al. (2014). On the other hand, the lower temperature estimation in the same work (82 K) is well consistent with ours.

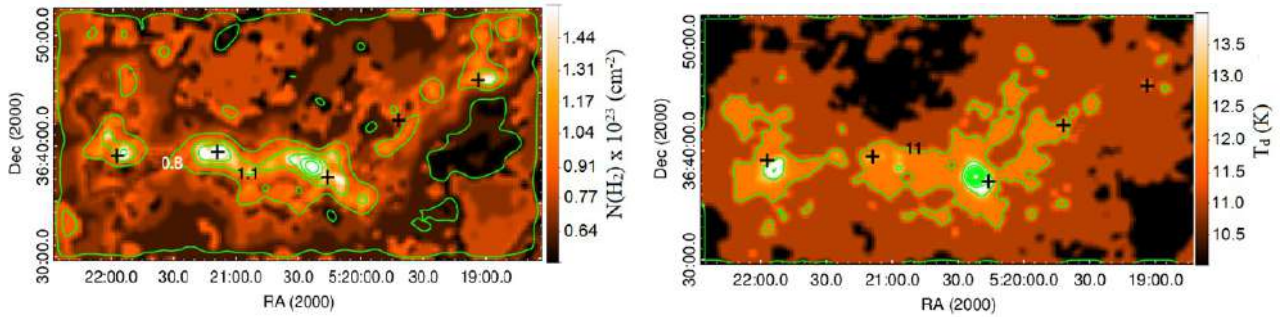


Figure 3. Maps of column density (*left panel*) and dust temperature (*right panel*) of IRAS 05168+3634 star-forming regions. On the $N(\text{H}_2)$ map the isodens corresponding to the values of 1.1×10^{23} and $0.8 \times 10^{23} \text{ cm}^{-2}$ shown. On T_d map isotherm corresponding to the value of 11 K is shown. The positions of IRAS sources are marked by crosses.

In the vicinity of IRAS 19111+1048, $N(\text{H}_2)$ is equal to $\sim 4 \times 10^{23} \text{ cm}^{-2}$ that well consistent with the data of multi transition ^{13}CO and CS observations in the G45.12+0.13 core (Churchwell et al., 1992). IRAS 19111+1048 itself is located in a region with a relatively high column density, which coincides in coordinates with counters of blueshifted emission of the bipolar molecular outflow (Hunter et al., 1997). It can be assumed that the outflow is the cause of the formation of the region with increased $N(\text{H}_2)$. It should be noted one more fact. One more region with a relatively high density and low temperature is located between the two UCHII regions. This region by coordinates coincides with the bridge between the UCHII regions, which is clearly distinguishable on *Herschel* colour-composite image (see Figures 1). This bridge is also clearly visible on the $\text{H}30\alpha$ map in Churchwell et al. (2010).

As can be seen in Figure 2, the temperature distribution in both UCHII regions has a pronounced spherical symmetry, and at a distance of 7 pix (~ 1.6 arcmin or ~ 3.7 pc) in G45.12+0.13 and 5 pix (~ 1.2 arcmin or 2.6 pc) in G45.07+0.13 from IRAS sources, the temperature decline almost stops. These distances correspond to 18 K isotherm and $2.9 \times 10^{23} \text{ cm}^{-2}$ isodense, after which the column density begins to increase rapidly. We can assume that it is the region where the influence of the stellar wind, leading to blowing of matter, ends. The total masses of these regions were calculated by Formula 4 for G45.12+0.13 region is $\sim 2.2 \times 10^5 M_\odot$ and for G45.07+0.13 is $10^5 M_\odot$.

It should be noted that the parameters obtained by the Modified blackbody model are not without certain errors (Harutyunyan et al., 2020). Among other causes the errors are a strong function of the parameters' values. In general, the χ^2 in the UCHII regions does not exceed 0.1. However, the uncertainty of parameters significantly increases in the regions with the maximum temperature, reaching a value of 0.8.

Table 1. The parameter of gas-dust matter and stellar content in the vicinity of IRAS sources

Parameter	05156+3643	05162+3639	05168+3634	05177+3636	05184+3635
Radius (arcmin)	2.8	0.25	3.0	3.5	2.5
YSO's number	47	5	57	79	52
$N(\text{H}_2) \times 10^{23} \text{ cm}^{-2}$	1.2	0.8	1.8	1.7	1.5
T_d (K)	12	12	24	13	14
$M(M_\odot)$ for $d = 1.9$ kpc	1.2×10^4	1.9×10^2	1.9×10^3	2.2×10^4	1.0×10^4
$M(M_\odot)$ for $d = 6.1$ kpc	1.4×10^5	2.2×10^3	2.1×10^4	2.5×10^5	1.2×10^5

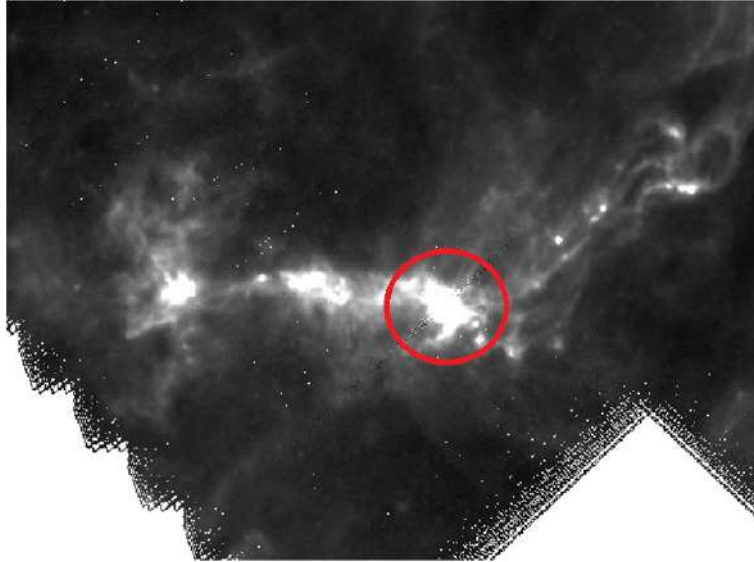


Figure 4. 2.5 level $250\ \mu\text{m}$ *Herschel* image of IRAS 05168+3634 star-forming region. The red circle marks the vicinity of IRAS 05168+3634 source.

3.2. IRAS 05168+3634 star-forming region

The final obtained column density and dust temperature maps of the wider region surrounding five IRAS sources (05168+3634, 05184+3635, 05177+3636, 05162+3639, and IRAS 05156+3643) are shown in Figure 3. In contrast to the previous region, this star-forming region stand out against of the environment not only with a higher temperature, but also with a higher density. In general, $N(\text{H}_2)$ in molecular clouds surrounding IRAS sources changes from $\sim 0.8 \times 10^{23}$ to $\sim 2.7 \times 10^{23}\ \text{cm}^{-2}$, and T_d from 11 to 26 K. We can see that the density in this star-forming region is only slightly less than in the previous one. However, the temperature of the gas-dust matter is much lower. Such a significant difference, of course, is primarily due to the stellar content. As mentioned above, stellar clusters in the UCHII regions include a significant number of high mass ZAMS stellar objects, accordingly with higher temperatures. In contrast, the subclusters in IRAS 05168+3634 star-forming region are mainly composed of younger, middle- and low-mass stellar objects with accordingly lower temperatures (Azatyan, 2019). The Table 1 lists some parameters that characterize both the stellar population and the gas-dust matter in the IRAS subclusters: the radii of the subclusters and the number of YSOs identified in them, as well as the hydrogen column density, dust temperature, and mass of the gas-dust component. Based on these data, a relationship is observed between the number of identified YSOs and the mass of the gas-dust component. Undoubtedly, the relationship between these parameters, including the evolutionary stage of the stellar objects, requires a more detailed study.

In general, in the molecular cloud, the uncertainty of parameters does not exceed 0.02. In general, the value of χ^2 is in this star-forming region noticeably lower than in the UCHII regions. This is most likely due to the fact that the temperature regime in this region is more suitable for the model we have applied. However, in the central part, in the vicinity IRAS 05168+3634, the uncertainty increases significantly, up to 0.9. In this case, this cannot be explained by the high temperature. The increase in the uncertainty of the parameters in this case is most likely explained by the quality of the images. Unfortunately, in all available *Herschel* images, this star-forming region is located at the very edge, where, of course, the image quality, especially in the $250\ \mu\text{m}$ channel, is not good enough. The Figure 4 clearly shows that in the area around the IRAS 05168+3634 source, even in a 2.5 level image, there are many bad pixels that, most likely, is the reason for the increase in the χ^2 value.

4. Conclusion

Thus, the study of ISM in both star-forming regions of showed that with a small difference in density, they differ significantly in temperature. Undoubtedly, this difference is interconnected with

the stellar composition. This once again confirms the well-known fact that any problem in astronomy, including the process of star formation, should be studied by a combination of many factors on the basis of extensive observational data, which can only be provided by survey observations made in different spectral ranges.

Acknowledgements

The authors are grateful to the organizers for holding the International Symposium "Astronomical Surveys and Big Data 2" and for publishing the paper.

References

- Azatyany N. M., 2019, *A&A*, **622**, A38
- Azatyany N., Nikoghosyan E., Harutyunian H., Baghdasaryan D., Andriasyan D., 2020, *ComBAO*, **67**, in press
- Battersby C., et al., 2011, *A&A*, **535**, A128
- Churchwell E., Walmsley C. M., Wood D. O. S., 1992, *A&A*, **253**, 541
- Churchwell E., Sievers A., Thum C., 2010, *A&A*, **513**, A9
- Han X. H., Zhou J. J., Wang J. Z., Esimbek J., Zhang J. S., Wang N., 2015, *A&A*, **576**, A131
- Harutyunyan H. A., Nikoghosyan E. H., Azatyany N. M., 2020, *Communications of the Byurakan Astrophysical Observatory*, **67**, 8
- Hernández-Hernández V., Zapata L., Kurtz S., Garay G., 2014, *ApJ*, **786**, 38
- Hildebrand R. H., 1983, *QJRAS*, **24**, 267
- Hunter T. R., Phillips T. G., Menten K. M., 1997, *ApJ*, **478**, 283
- Launhardt R., et al., 2013, *A&A*, **551**, A98
- Molinari S., Brand J., Cesaroni R., Palla F., 1996, *A&A*, **308**, 573
- Molinari S., et al., 2016, *A&A*, **591**, A149
- Rivera-Ingraham A., et al., 2010, *ApJ*, **723**, 915
- Sakai N., Honma M., Nakanishi H., Sakanoue H., Kurayama T., Shibata K. M., Shizugami M., 2012, *PASJ*, **64**, 108
- Varricatt W. P., Davis C. J., Ramsay S., Todd S. P., 2010, *MNRAS*, **404**, 661
- Vig S., Ghosh S. K., Kulkarni V. K., Ojha D. K., Verma R. P., 2006, *ApJ*, **637**, 400
- Wood D. O. S., Churchwell E., 1989, *ApJS*, **69**, 831
- Wu Y. W., et al., 2019, *ApJ*, **874**, 94